



Trans. Nonferrous Met. Soc. China 34(2024) 3151-3169

Transactions of **Nonferrous Metals** Society of China





Strengthening mechanism of T8-aged Al-Cu-Li alloy with increased pre-deformation

San-xi DENG¹, Jin-feng LI¹, Li WANG², Yue-yan CHEN², Zheng-wu XIANG¹, Peng-cheng MA³, Yong-lai CHEN³, Dan-yang LIU¹

- 1. School of Materials Science and Engineering, Central South University, Changsha 410083, China; 2. Southwest Aluminum (Group) Co., Ltd., Chongqing 401326, China;
 - 3. Aerospace Research Institute of Materials and Processing Technology, Beijing 100076, China

Received 30 June 2024; accepted 12 September 2024

Abstract: The microstructure evolution and mechanical properties of a T8-aged Al-Cu-Li alloy with increased pre-deformation (0-15%) were investigated, revealing the microstructure-strength relationship and the intrinsic strengthening mechanism. The results show that increasing the pre-deformation levels remarkably improves the strength of the alloy but deteriorates its ductility. Dislocations introduced by pre-deformation effectively suppress the formation of Guinier-Preston (GP) zones and provide more nucleation sites for T1 precipitates. This leads to more intensive and finer T1 precipitates in the samples with higher pre-deformation levels. Simultaneously, the enhanced precipitation of T1 precipitates and inhibited formation of GP zones cause the decreases in number and sizes of θ' precipitates. The quantitative descriptions of the strength contributions from different strengthening mechanisms reveal that strengthening contributions from T1 and θ' precipitates decrease with increasing pre-deformation. The reduced diameters of T1 precipitates are primarily responsible for their weakened strengthening effects. Therefore, the improved strength of the T8-aged Al-Cu-Li alloy is mainly attributed to the stronger strain hardening from the increased pre-deformation levels.

Key words: Al-Cu-Li alloy; pre-deformation; precipitation; strength; strengthening mechanism

1 Introduction

When considering the demands of lightweight and energy-saving, aluminum-lithium (Al-Li) alloys have gained substantial attention in aerospace industries due to their low density, high specific strength and stiffness [1-4]. However, the previous generations of Al-Li alloys characterized by high Li content (>2.0 wt.%) are defective in and toughness, thereby restricting their applications [5–7]. By adjusting the Cu (>3.0 wt.%) and Li (<2.0 wt.%) contents as well as supplementing with various microalloying elements, such as Mg, Ag, and Zn, the 3rd generation Al-Cu-Li alloys have achieved great improvement in their mechanical properties and therefore successfully serve in aircraft and aerospace structures [8-13]. As age-hardenable alloys, the mechanical properties of Al-Cu-Li alloys are largely dependent on their precipitates. Generally, T1-Al₂CuLi and θ'-Al₂Cu precipitates predominant in these alloys, and meanwhile, they are accompanied by a few δ' -Al₃Li and S'-Al₂CuMg precipitates [14-17]. In addition, the GP zones and δ'/GP zone/ δ' composite precipitate are also found [18–21]. Compared with the others, the highaspect-ratio T1 precipitates on {111}_{A1} habit plane are recognized as the most effective strengthening precipitates because of their greater hindrance for the movement of the dislocation [22–24].

Microalloying is known as an effective method for enhancing the properties of Al-Cu-Li-based alloys through the trace addition of some elements to alter the precipitation characteristics. Additionally, reasonable thermomechanical processing is also vital to optimize the mechanical properties of Al-Cu-Li alloys. In general, 2%-5% predeformation before artificial aging (AA) is usually involved in the traditional processes for aerospace applications of Al alloys to release residual stresses from quenching [25]. Moreover, extensive studies have demonstrated that dislocations introduced by the pre-deformation can provide homogeneous nucleation sites for T1 precipitates and therefore promote the T1 precipitation, improving the alloy strength [26–29]. On the other hand, the enhanced precipitation of T1 precipitates at the interior of grains instead weakens the formation of the GBs precipitates, which favors the improvement of ductility [30,31]. Consequently, influences of pre-deformation on the precipitation behavior and the resultant mechanical properties of Al-Cu-Li alloy have drawn extensive attention.

WANG et al [32] discovered that introducing 3.0% pre-deformation in an Al-Cu-Li-Mg-Ag alloy suppressed the formation of GP zones during the early aging stage, but significantly accelerated the aging kinetics and growth rate of T1 precipitates. Quantitative analysis of T1 and θ' precipitates in a 2A55 Al-Li alloy at various levels of predeformation was conducted by ZENG et al [26], revealing a notable increase in T1 precipitates while a decrease in θ' precipitates. However, it was found that benefits from pre-deformation reached saturation at around 6%-9% [33,34]. DUAN et al [35] claimed that the precipitation kinetics of T1 precipitates was continually accelerated by increasing the pre-stain and attributed the improvement of strength for the alloy to the more T1 precipitates and stronger strain hardening effect. LI et al [36] reported that as the level of pre-rolling deformation reached 20%, the atomic diffusion channels were reduced due to dislocation entanglement, and therefore the number density of T1 precipitates and the strength of the alloy decreased. Based on the shear mechanism with respect to the monolayer T1 precipitate, RODGERS and PRANGNELL [37] found that as predeformation levels increased, the enhanced strain hardening compensated for the loss of precipitation strengthening due to the decreasing diameter of T1 precipitates, thereby improving the strength of the alloy. The strengthening mechanisms of precipitates are largely decided by their morphological parameters. It has been demonstrated that the transformation of the shearing mechanism to the bypassing mechanism would occur for the T1 precipitates with a large diameter (>100 nm) and thickness (>1.3 nm) [32,38,39]. Although many efforts are focused on the effects of pre-deformation, there are few reports about the large strain of pre-deformation. Meanwhile, the strengthening contributions of θ' precipitates and the variation of base strength during the aging process also should be fully considered, which were neglected in many studies about the strengthening models of Al-Cu-Li-baesd alloys.

This work focuses on revealing the evolution of strengthening contribution mechanisms of a T8-aged Al-Cu-Li alloy with increased predeformation (up to 15.0%) by investigating the evolution of microstructures and mechanical properties. Pre-deformation-introduced dislocations were characterized by X-ray diffraction (XRD) and transmission electron microscopy (TEM). Based on the TEM observation, the characteristics of the main precipitates (T1 and θ' precipitates) were quantitively analyzed, and resultant strengthening contributions were calculated. Furthermore, the relationship among microstructures, strengthening mechanisms, and mechanical properties were discussed. The findings will theoretical guidance for the practical production of high-strength Al-Cu-Li alloys.

2 Experimental

2.1 Materials preparation and heat treatment procedures

The Al-Cu-Li alloy was supplied by Southwest Aluminum (Group) Co., Ltd., China. The as-received alloy was 21 mm-thick hot-rolled plate. The chemical compositions of the plate samples are detailed in Table 1. The rolling direction (RD), transverse direction (TD), and normal direction (ND) of the plate are defined in Fig. 1(b). Tensile

Table 1 Chemical compositions of experimental Al–Cu–Li alloy (wt.%)

Cu	Li	Mg	Ag	Zr	Fe	Si	Al
3.95	0.92	0.36	0.36	0.12	0.06	0.02	Bal.

test specimens were extracted from the 1/2 plate thickness along the RD. The sampling positions and dimensions of tensile test specimens are illustrated in Figs. 1(b) and 1(c), respectively.

Figure 1(a) presents a schematic illustration of the entire experimental process and heat treatment process of the alloy. Initially, all specimens underwent a solid solution treatment at 510 °C for 1 h. Subsequently, some specimens were cooled to 148 °C in the furnace with a cooling rate of 40 °C/h and insulated at this temperature for 2 h (referred to as the SFCI samples). The remaining specimens were immediately quenched in room-temperature water (designated as the SQ sample). Some SQ samples were aged at 148 °C for 38 h to achieve the T6 samples. Additionally, other SQ samples were

subjected to various levels of pre-deformation through stretching (termed as T3 samples) and then were artificially aged at 148 °C for 38 h to obtain the T8 samples. The pre-deformation amounts were 3.0%, 6.0%, 9.0%, 12.0% and 15.0%, respectively. On this basis, the obtained T3 and T8 samples were defined as T3-X and T8-X samples, respectively, where X represents the pre-deformation amounts. Table 2 gives the denoted names of the samples that suffered different heat treatment procedures. To avoid the occurrence of natural aging (NA), the SQ samples and T3-X samples were immediately (within 10 min) subjected to tensile tests after solid solution treatment and pre-deformation.

2.2 Tensile tests

The pre-deformation and tensile tests were performed on an MTS-810 universal mechanical testing machine at room temperature with a tensile rate of 2.0 mm/min according to the ASTM-E8 standard. The strain of the samples was monitored using a 25.0 mm extensometer. To ensure accuracy

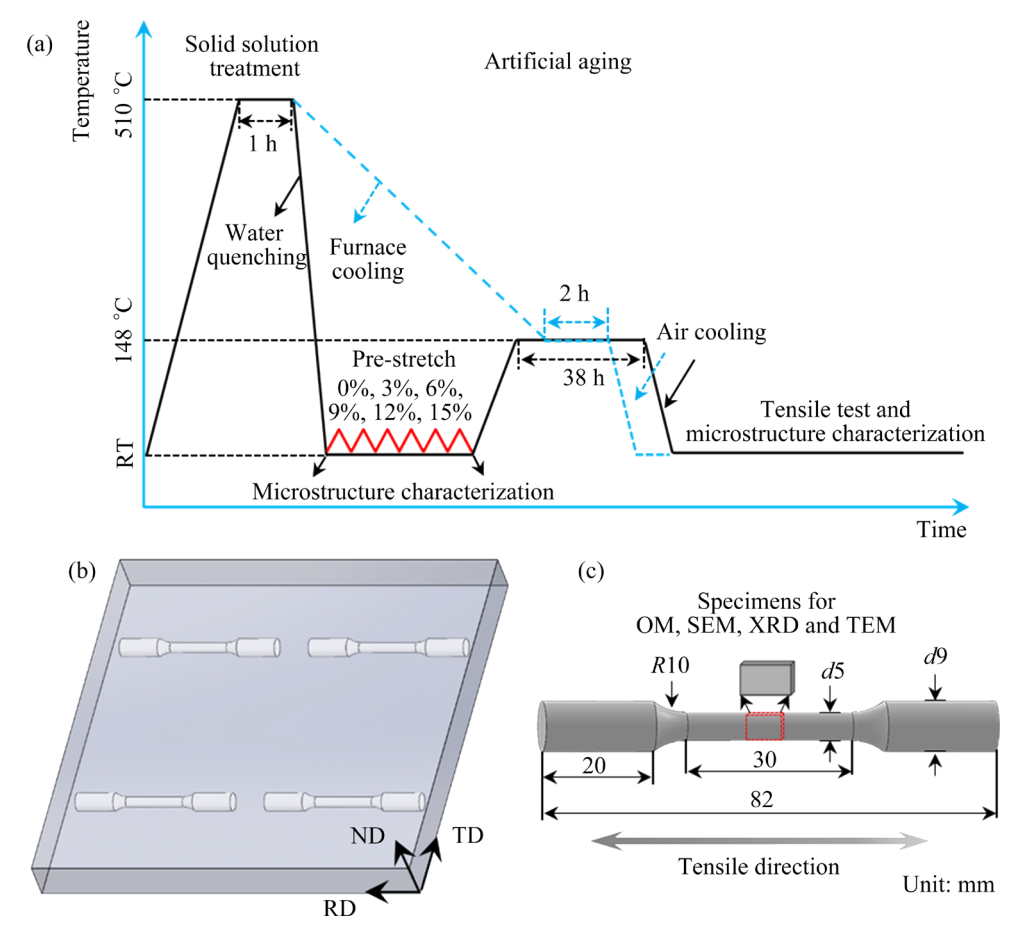


Fig. 1 Schematic diagram of whole experimental route and heat treatment procedure (a); Sampling position of tensile test specimens in as-received plates (b); Dimensions of tensile test specimens and sampling position of specimens for microstructure characterization (c)

Table 2 Designations of samples subjected to different heat treatments

Sample	Heat treatment procedure				
SQ	Solid solution treatment (510 °C, 1 h) + Water quenching				
SFCI	Solid solution treatment (510 °C, 1 h) + Furnace cooling to 148 °C + Insulation treatment (148 °C, 2 h)				
Т3-Х	Solid solution treatment (510 °C, 1 h) + Water quenching + Pre-deformation (3.0%, 6.0%, 9.0%, 12.0%, and 15.0%)				
Т6	Solid solution treatment (510 °C, 1 h) + Water quenching + Aging treatment (148 °C, 38 h)				
T8- <i>X</i>	Solid solution treatment (510 °C, 1 h) + Water quenching + Pre-deformation (3.0%, 6.0%, 9.0%, 12.0%, and 15.0%) + Aging treatment (148 °C, 38 h)				

of the results, at least three tensile specimens corresponding to each heat treatment condition were tested and the average value was adopted. The fracture morphologies of the tensile test specimens were examined by a scanning scanning electron microscope (SEM).

2.3 Microstructure characterization

Specimens for microstructure characterization were obtained from the parallel segment of the tensile test specimens along the RD, as presented in Fig. 1(c). The specimens for metallographic analysis underwent sequential grinding, polishing, and anodic treatment before observation using a Leica DMI300 M optical microscope (OM). The distribution and chemical compositions of secondary phase particles were examined using a scanning electron microscope (SEM, Regulus 8230) equipped with energy-dispersive spectroscope (EDS) in backscattering (BSE) mode. The metallographic and SEM observations were conducted on the longitudinal sections (RD-ND) of plates. A FEI Talos F200X transmission electron microscope (TEM) with a high-angle annular dark field (HAADF) detector was employed to observe the precipitate characteristics and dislocation configurations. The thickness of TEM observation region was determined through convergent beam electron diffraction (CBED) [40,41]. Additionally, the X-ray diffraction (XRD) measurement was utilized to quantitatively analyze the dislocations of different samples. It was carried out on a Rigaku SmartLab high-resolution XRD instrument with a 2θ range of 10°–140°, operating at 40.0 kV and a scanning speed of 2 (°)/min. Further detailed quantification process of the dislocation density can be found in our previous study [42]. TEM specimens were prepared by the twin-jet electropolishing method, where specimens were thinned to approximately 80.0 μm and punched into circular foils with 3.0 mm in diameter. After that, the foils were subjected to twin-jet electropolishing treatment in a mixture of 75 vol.% methanol and 25 vol.% nitric acid at the temperature from −20 to −30 °C and a voltage of about 15.0 V.

3 Results

3.1 Mechanical properties

Figure 2 shows the engineering stress-strain curves and corresponding mechanical properties of different samples. As depicted in Fig. 2(a), evident Portevin-Le Chatelier (PLC) effects associated with plastic instability are observed in the SQ and T3-X samples, which are derived from the interaction between dislocations and solute atoms [43-45]. Notably, fluctuations different from the T3-X samples are also presented in the stress-strain curve of the SFCI sample, which is mainly related to the coarse phases at grain boundaries (GBs) formed during the furnace cooling stage [46,47]. The yield strength (YS), ultimate tensile strength (UTS), and elongation (EL) of SFCI sample are 104.6 MPa, 238.8 MPa, and 16.0%, respectively, which are significantly lower than those of the SQ sample (165.8 MPa, 351.8 MPa and 22.0%), as shown in Fig. 2(b). In addition, with improving the predeformation levels, the YS of the T3-X samples shows an almost linear increase while a retarded increase in UTS. Meanwhile, the EL tends to decrease rapidly. Compared to the SQ sample, the YS of the T3-3 sample is increased by about 70.8 MPa, which is from the strain hardening induced by pre-deformation. The strain hardening values of samples at various pre-deformation levels can be determined by subtracting the YS of the SQ sample from the YS of the T3-X sample. By calculating, it increases from 70.8 MPa in the T3-3 sample to 257.5 MPa in the T3-15 sample. The result indicates that the strain-hardening effect is

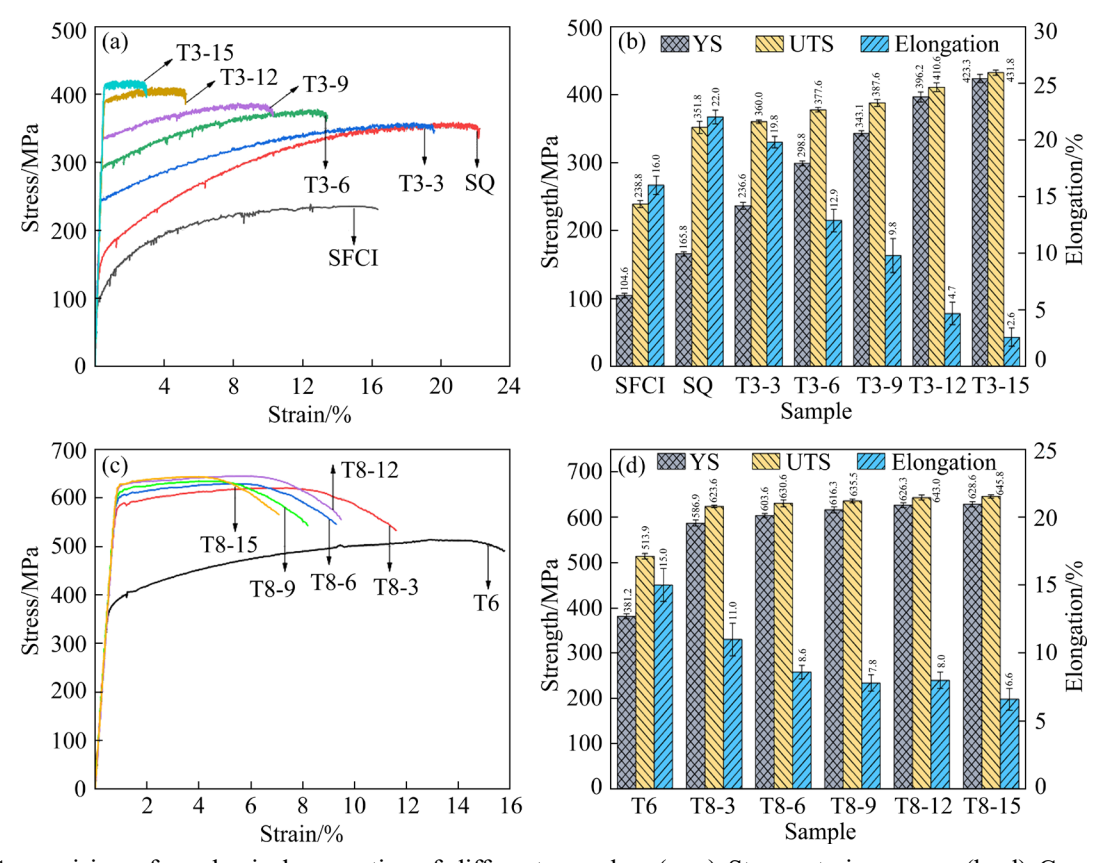


Fig. 2 Comparision of mechanical properties of different samples: (a, c) Stress-strain curves; (b, d) Corresponding mechanical properties

significantly enhanced by the improvement of pre-deformation levels.

As shown in Fig. 2(c), PLC effects completely disappear in the stress-strain curves of the AA samples (T6 and T8 tempers). This indicates that the solute atoms in the matrix are almost depleted during the AA process. As indicated in Fig. 2(d), the YS and UTS increase from 381.2 and 513.9 MPa in the T6 sample to 603.6 and 630.6 MPa in the T8-6 sample, respectively, showing a rapid strength improvement. However, the EL decreases from 15.0% in the T6 sample to 8.6% in the T8-6 sample. Further pre-deformation exceeding 6.0% in the samples induces a retarded strength increment. In the T8-15 sample, the YS, UTS, and EL are 628.6 MPa, 645.8 MPa, and 6.6%, respectively. These results suggest that increasing predeformation significantly enhances the alloy's strength but deteriorates its elongation.

Figure 3 shows the typical morphologies of tensile fracture of different AA samples. As presented in Fig. 3(a), deep dimples accompanied by some secondary phase particles at the bottom (indicated by the yellow arrows) are dominant on

the fracture surface of the T6 sample. The T8-3 sample exhibits a similar morphology, but the proportion of the deep dimples decreases and a few shallow dimples emerge (indicated by the white arrows), as shown in Fig. 3(b). These indicate that transgranular fracture mode is predominant in the T6 and T8-3 samples, corresponding to their relatively high EL. Nevertheless, for the samples with pre-deformation above 6.0%, the fracture mode is different. As shown in Figs. 3(c-f), the fracture surfaces of different samples are covered with the predominant cleavage planes and local shallow dimples, indicating an intergranular-dimple mixed fracture mode.

3.2 Microstructure

3.2.1 Microstructures of pre-treatment samples

Figure 4 displays the microstructures of the SQ and SFCI samples. It can be observed from Figs. 4(a, c) that there are no obvious differences in the grain morphology between the two samples. Both samples exhibit fiber-like grains with an average thickness of about 20.0 μm, accompanied by some fine equiaxed grains at the grain boundaries

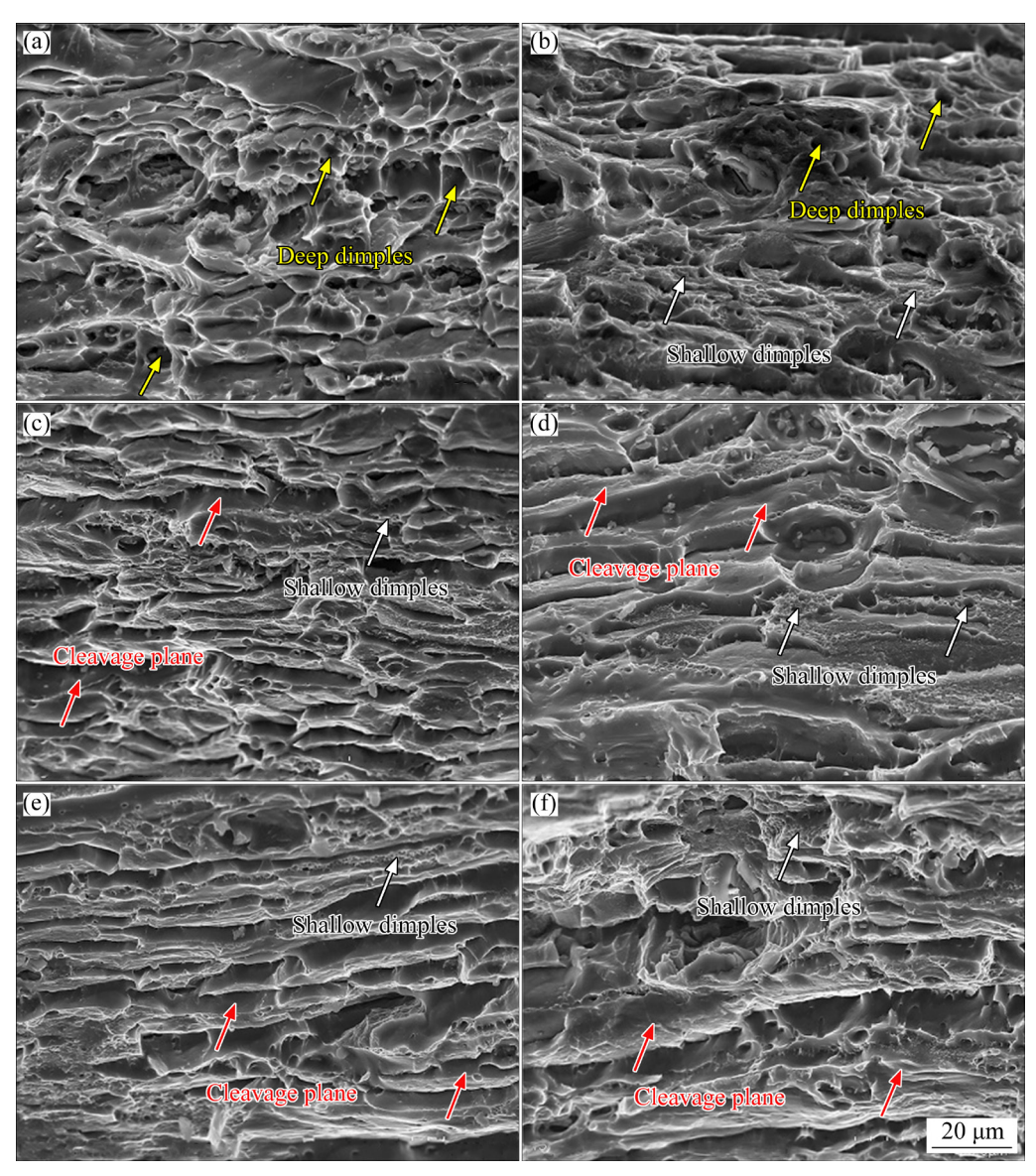


Fig. 3 Typical tensile fracture morphologies of different samples: (a) T6; (b) T8-3; (c) T8-6; (d) T8-9; (e) T8-12; (f) T8-15

(GBs). This indicates that the SFCI treatment has little impact on the grain morphology. In Fig. 4(a), a few black secondary phases remain at the GBs of the SQ sample, while no evident secondary phases are found inside the grains, suggesting the successful solid solution treatment. Conversely, Fig. 4(c) shows strip-like black/white secondary phases densely distributed within the grains of the SFCI sample with massive large-size secondary phases along the GBs. The OM observation results are further supported by the BSE images of samples. In Fig. 4(b), only a few small white secondary phases, identified as Cu-rich phases through EDS analysis, are presented at the GBs of the SQ sample. On the other hand, Fig. 4(d) reveals significantly

larger and denser secondary phases in the SFCI sample. Among them, the bulk phases are mainly distributed at the GBs, while the striped phases are concentrated within the grains. As evidenced by the EDS analysis in Figs. 4(e, f), all these phases are also primarily enriched in Cu elements. Similar results have also been reported by DUAN et al [48]. As for the SFCI sample, the slow cooling rate enables the massive formation of secondary phases, which therefore almost depletes the solute atoms in the matrix.

To investigate the evolution of dislocation configurations and density in samples with increasing pre-deformation, a combination of TEM and XRD measurements is employed to analyze

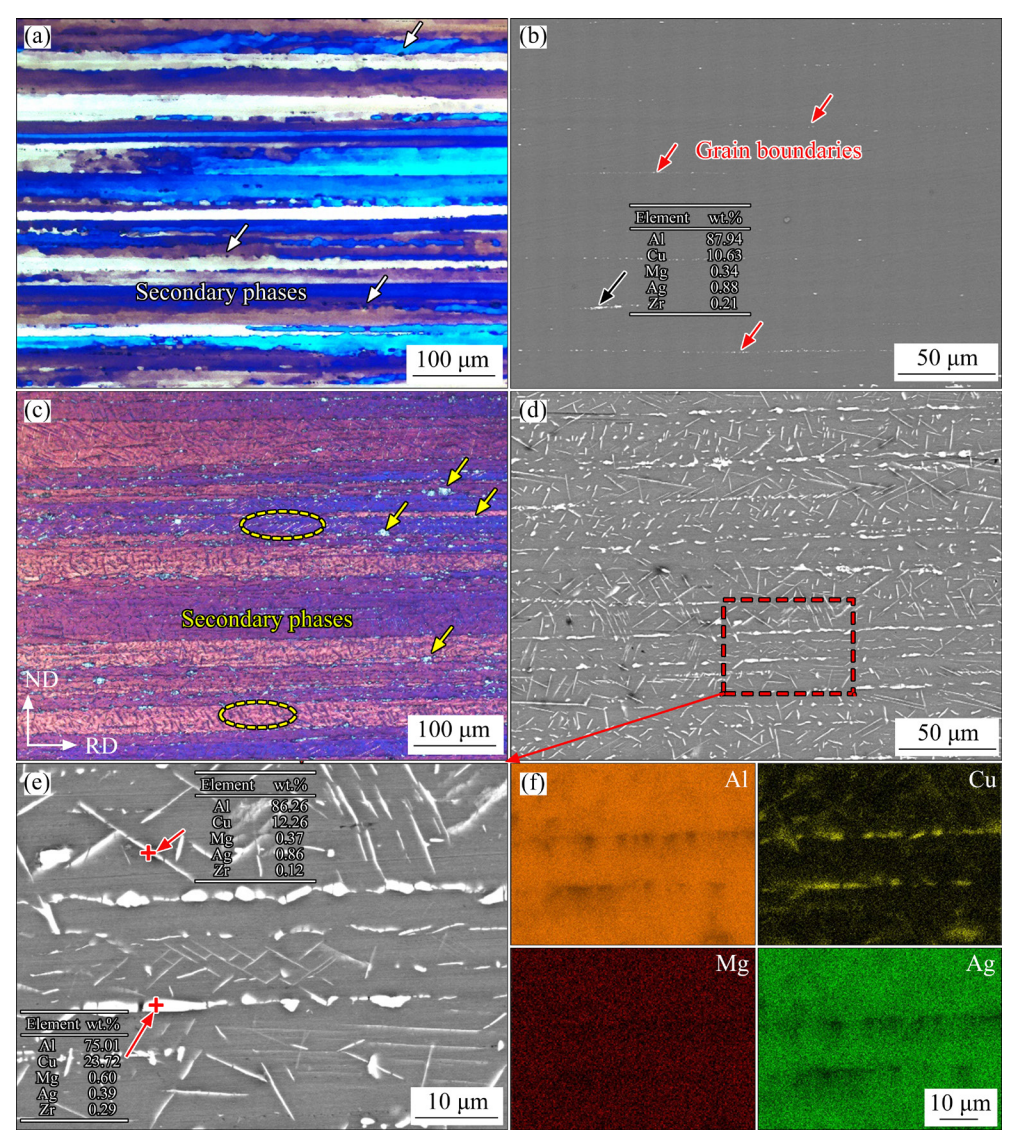


Fig. 4 Microstructures of SQ (a, b) and SFCI (c, d, e, f) samples: (a, c) OM images showing typical grain morphologies; (b, d, e, f) BSE images showing distribution and chemical compositions of secondary phases; (e) Enlarged view of region of red dotted frame in (d); (f) EDS-mapping images corresponding to (e)

microstructures. Figure 5 illustrates comparison of dislocation configurations in samples at various pre-deformation levels. As shown in Figs. 5(a, e), almost no obvious dislocations are found in the SQ sample, except for a few Zr-rich spherical dispersoids. According to our previous studies [49,50], these dispersoids are identified as the Al₃Zr particles. In contrast, samples subjected to pre-deformation exhibit abundant wavy lines with black contrast (indicated by the red arrows) and fine ring-like structures (indicated by the yellow arrows), as shown in Figs. 5(b-d). These structures are indeed the projections of three-dimensional dislocations and dislocation loops. Figure 5(b) reveals that spare and homogeneous dislocations are distributed in the T3-3 sample, in which the dislocations lines are predominant. Differently, the T3-9 and T3-15 samples display significantly increased dislocations, which tangle with each other to form dense network structures, as shown in Figs. 5(c, d). Meanwhile, an evident increase in the fine dislocation loops is also observed.

The XRD data were analyzed using the Williamson–Hall method to quantitatively assess the dislocation density in different samples. Figures 6(a-c) display the XRD patterns, Williamson–Hall plots, and the dislocation density of different samples. As expected, dislocation density rapidly increases with improving the pre-deformation levels, which increases from 0.8×10^{14} m⁻² in the T3-3

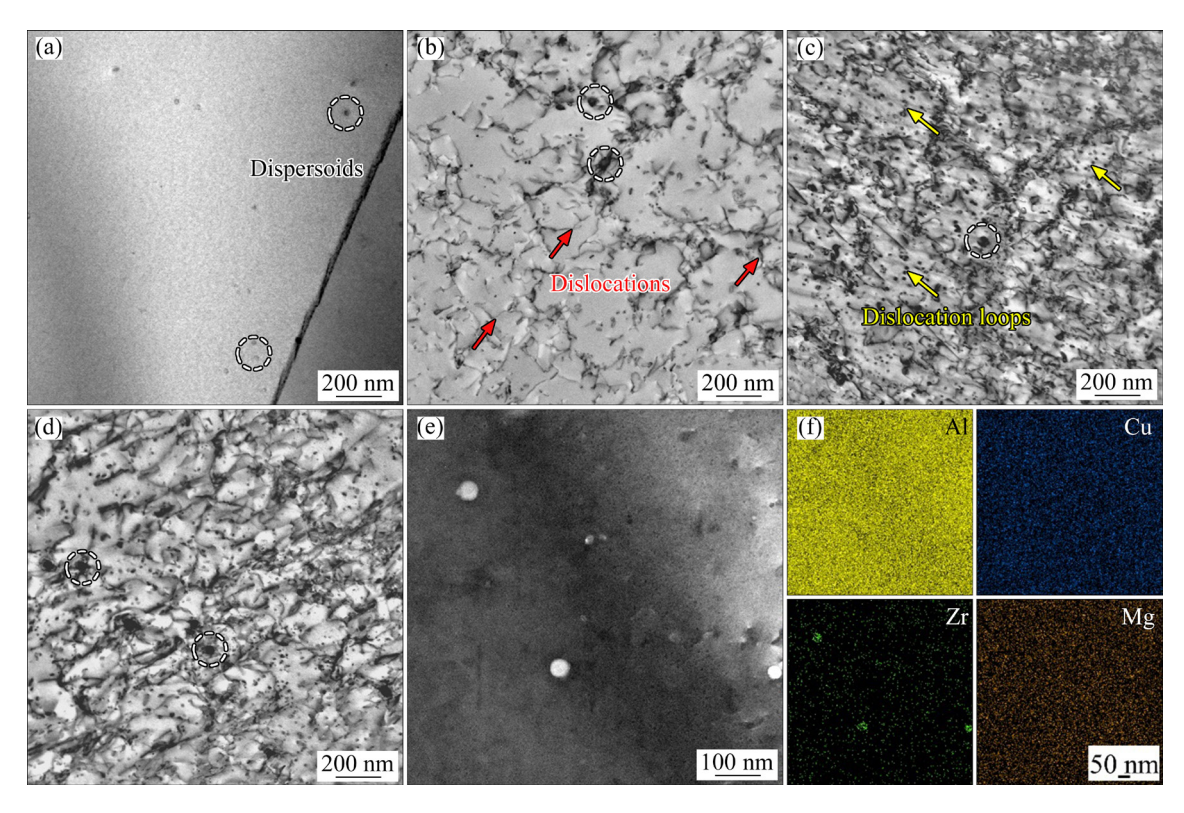


Fig. 5 STEM images (a–d) showing dislocations configuration in different samples and STEM-EDS mappings (e, f) showing compositions of typical dispersoids in samples: (a, e, f) SQ sample; (b) T3-3 sample; (c) T3-9 sample; (d) T3-15 sample

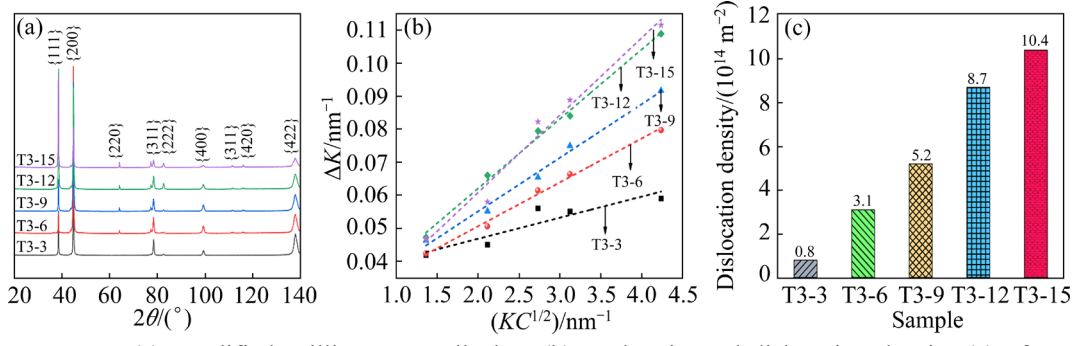


Fig. 6 XRD patterns (a), modified Williamson-Hall plots (b), and estimated dislocation density (c) of samples with different pre-deformation levels

sample to about $10.4 \times 10^{14} \, \text{m}^{-2}$ in the T3-15 sample. These findings suggest that increasing the pre-deformation levels in samples not only alters the dislocation configurations but also markedly increases the dislocation density.

3.2.2 Precipitation behaviors of AA samples

Figure 7 shows the selected area electron diffraction (SAED) patterns viewed along the [110]_{Al} zone axis for AA samples with different pre-deformation levels and the corresponding schematical diagram illustrating the SAED pattern model of the Al–Cu–Li alloys. In the SAED

patterns, streaks from the T1 precipitates, θ' precipitates, and GP zones are highlighted by red and yellow dashed circles, respectively. The T6 sample displays distinct streaks from the T1 precipitates passing through $[\bar{1}11]_{A1}$ and $[1\bar{1}1]_{A1}$ spots, as well as continuous streaks with high intensity through the $[002]_{A1}$ spot, as depicted in Fig. 7(a). These findings suggest the coexistence of a high density of GP zones, θ' precipitates, and T1 precipitates in the T6 sample. In comparison, the T8-X samples exhibit stronger streaks of T1 precipitates, as shown in Figs. 7(b–e), suggesting

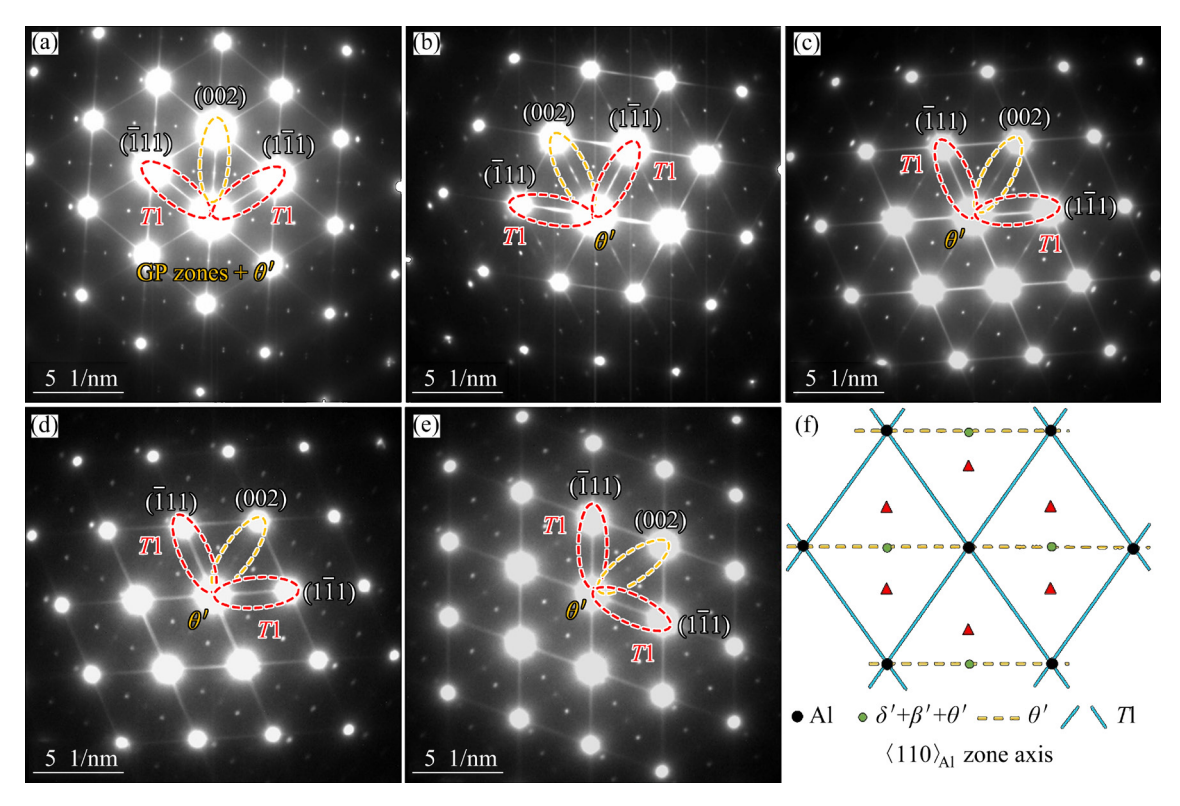


Fig. 7 Selected area electron diffraction (SAED) patterns of different AA samples recorded along [110]_{Al} zone axis: (a) T6; (b) T8-3; (c) T8-6; (d) T8-12; (e) T8-15; (f) Schematical diagram of diffraction spots and streaks derived from main precipitates in [110]_{Al} zone axis

the enhanced precipitation of T1 precipitates with the increased pre-deformation. Notably, the streaks through $[002]_{A1}$ spot become discontinuous and weak, and almost completely disappear as the pre-deformation levels are improved. This implies that pre-deformation suppresses the formation of GP zones and meanwhile, exerts a strong inhibition effect on the precipitation of θ' precipitates as the pre-deformation increases.

Figure 8 exhibits the HAADF-STEM images of different AA samples viewed along the [110]_{A1} zone axis. In Fig. 8(a), it is observed that some T1 precipitates of large sizes and a few Al₃Zr particles inhomogeneously distribute in the T6 sample. Additionally, a high density of small-sized GP zones and a few large θ' precipitates are formed intensively in regions where the T1 precipitates are less. Nevertheless, as revealed by Figs. 8(b-f), no GP zones are found in the T8-X samples and the T1 precipitates are predominant, accompanied by some θ' precipitates. Moreover, increasing the pre-deformation results in a significant rise in the number of T1 precipitates and a decrease in their size, while the number and sizes of θ' precipitates

decrease noticeably. These results, in combination with SAED findings, suggest that pre-deformation effectively suppresses the formation of GP zones. Furthermore, the higher pre-deformation levels in samples promote the precipitation of T1 precipitates but reduce their size, while decrease the number and sizes of θ' precipitates.

According to the obtained HAADF-STEM images, the characteristics of T1 and θ' precipitates are quantitively analyzed. According to literature, for the TEM images recorded along the [110]Al zone axis, both T1 and θ' precipitates can be simultaneously observed, in which only two of four T1 variants and one of three θ' variants can be observed, presenting needle-like shape [51,52]. Consequently, the factor of the variants for T1 and θ' precipitates is also fully considered. For each sample, at least 5 images containing more than 200 precipitates are manually measured by using the Image J software. Figure 9 presents the size distribution, average diameter, and number density of T1 and θ' precipitates in different samples. As shown in Figs. 9(a-f), the size distribution ranges of T1 and θ' precipitates are remarkably narrowed

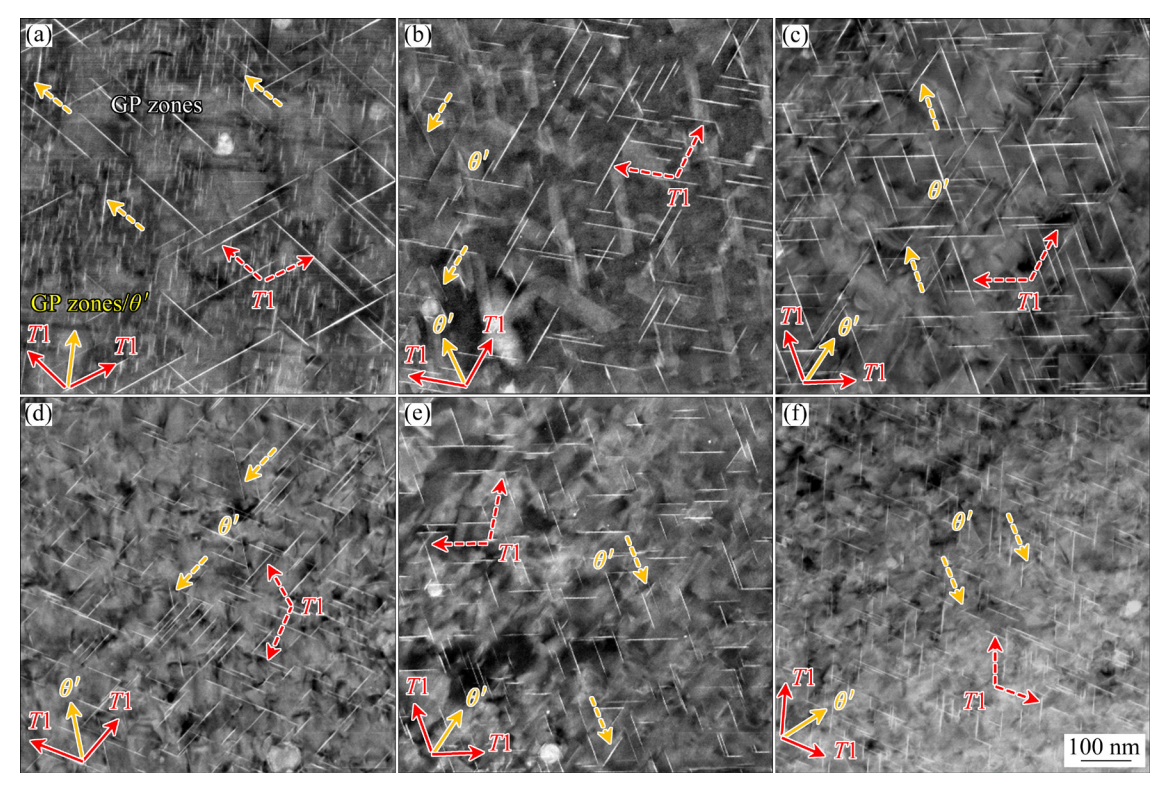


Fig. 8 HAADF-STEM images of different AA samples viewed along [110]_{Al} zone axis: (a) T6; (b) T8-3; (c) T8-6; (d) T8-9; (e) T8-12; (f) T8-15

with increasing the pre-deformation levels in samples. Meanwhile, the average diameter of T1 precipitates decreases from 112.3 nm in the T6 sample to 42.8 nm in the T8-15 samples, while their number density increases from 806 to 13800 µm⁻³, as indicated in Figs. 9(g, h). The θ' precipitates in the T6 sample exhibit a large average diameter (143.4 nm) whereas a relatively low number density (282 μm⁻³). With improving the pre-deformation levels, the T8-X samples show a continuous decrease in the average diameter and number density of θ' precipitates. These findings indicate that increasing pre-deformation improves the homogeneity of the precipitates and enhances the precipitation of T1 precipitates while diminishes the precipitation of the θ' precipitates and decreases the diameter of the precipitates.

Figure 10 exhibits high-resolution transmission electron microscopy (HRTEM) images of different samples viewed along [110]_{Al} zone axis. To assess the thickness of precipitates in different samples, at least 15 independent precipitates for each sample are measured and the statistical results are listed in Table 3. The thickness of θ' precipitates in the samples remains relatively constant, at 2.40 nm

approximately. In the T6 sample, the thickness of T1 precipitates is about 1.86 nm. Comparatively, the T8-X sample shows a slight decrease in the thickness of T1 precipitates, stabilizing at 1.2–1.4 nm.

Figure 11 displays the HAADF-STEM images of the GB/sub-grain boundary and the adjacent regions in different samples. In the T6 sample, dense T1 precipitates with large sizes continuously distribute at the grain boundaries (GBs) and evident precipitation-free zones (PFZs) observed, as presented in Fig. 11(a). However, almost no PFZs are presented around the sub-grain boundaries in the T8-X samples, as depicted in Figs. 11(b-d). As for the T8-X samples, more nucleation sites for T1 precipitates provided by pre-deformation make the distribution of T1 precipitates in grains more uniform, which effectively eliminates the PFZs. Meanwhile, the T1 precipitation around the sub-grain boundaries competes with the sub-grain boundary precipitates. As a result, the T1 precipitates at sub-grain boundaries in the T8-X samples exhibit a much smaller size and transform to discontinuous, as shown in Figs. 11(b-d).

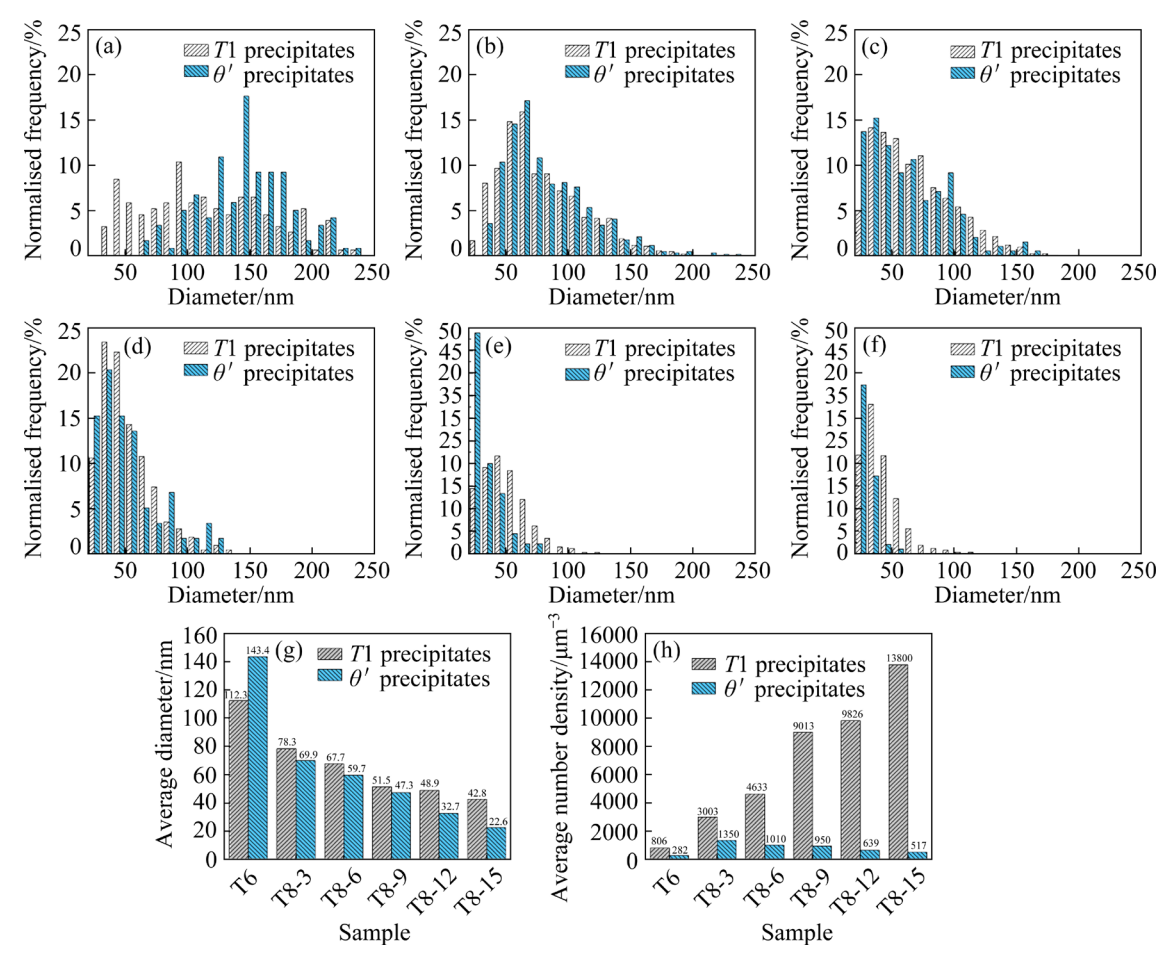


Fig. 9 Size distribution (a-f), average diameter (g), and average number density (h) of T1 precipitates and θ' precipitates in different AA samples: (a) T6; (b) T8-3; (c) T8-6; (d) T8-9; (e) T8-12; (f) T8-15

4 Discussion

4.1 Effect of pre-deformation on precipitation behaviors

The above results demonstrate that samples with different pre-deformation levels exhibit considerably distinct precipitation behaviors. The T6 sample presents intensively distributed small-size GP zones, whereas they almost completely disappear in the T8-X samples, as illustrated in Figs. 7 and 8. This observation is consistent with the previous studies by ZENG et al [42] and WANG et al [32]. Indeed, this precipitation behavior is primarily attributed to the pre-deformation prior to AA. During the early stage of aging, Mg atoms with higher binding energy preferentially bond with quenched-in vacancies to form Mg-vacancy complexes. Due to the strong Mg-Cu interactions, these complexes tend to trap Cu atoms, leading

to the formation of Mg-Cu co-clusters, which eventually aggregate and grow into the Cu-rich GP zones [53]. The formation of GP zones is highly susceptible to the concentration of quench-in vacancy in the matrix [44,54]. However, it has been revealed that vacancies are prone to annihilation at moving dislocations [55,56]. In the T8-X samples, the high density of dislocations introduced by pre-deformation inevitably decreases the vacancy concentration, thereby suppressing the formation of GP zones. On the other hand, the dislocations from pre-deformation are also primarily responsible for the enhanced precipitation of T1 precipitates. As we know, the pre-deformation-introduced dislocations can act as homogeneous nucleation sites for T1 precipitates. As confirmed by the TEM observation and XRD results (Figs. 5 and 6), dislocations in samples significantly increase with improving the pre-deformation levels. More nucleation sites of T1 precipitates provided by the increased dislocations

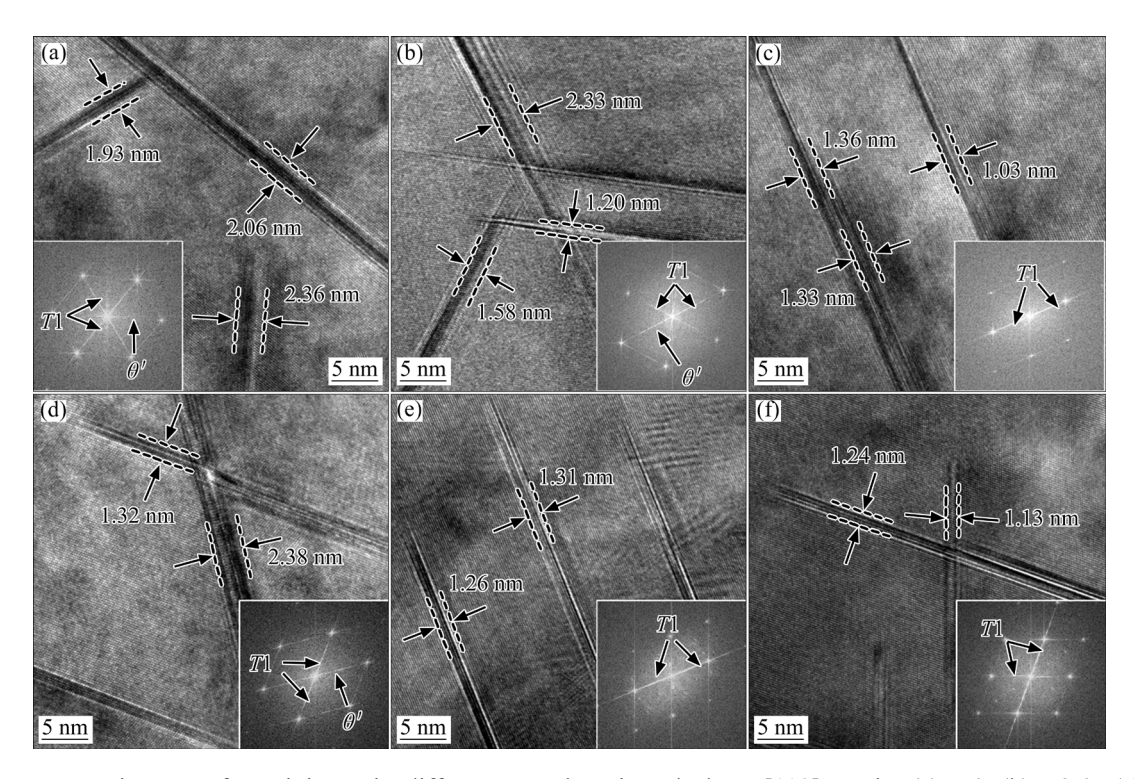


Fig. 10 HRTEM images of precipitates in different samples viewed along [110]_{Al} axis: (a) T6; (b) T8-3; (c) T8-6; (d) T8-9; (e) T8-12; (f) T8-15 (The inserted images show corresponding fast Fourier transformation (FFT) patterns)

Table 3 Average thickness of *T*1 precipitates in different samples (nm)

T6	T8-3	T8-6	T8-9	T8-12	T8-15
1.86	1.35	1.36	1.32	1.29	1.27

eventually cause the higher density of T1 precipitates in samples with higher pre-deformation levels (Figs. 7 and 8). Furthermore, the formation of T1 and θ' precipitates competes with each other for solute atoms during the aging process. In the T8-X samples, the increased pre-deformation inhibits the formation of the precursor GP zones of the θ' phase but promotes T1 precipitation, which ultimately leads to a decrease in the number density of θ' precipitates (Figs. 7-9). Nevertheless, the high density of T1 precipitates narrows the interprecipitate spacing and diffusion field around independent precipitates, restricting their growth. As a result, the diameter and size distribution of T1 and θ' precipitates decrease in samples with higher pre-deformation levels (Fig. 9).

4.2 Relationship between microstructures and strengthening contributions

The mechanical properties of alloys are largely dependent on their microstructure. As discussed in

Section 4.1, increasing the pre-deformation levels in samples remarkably alters the precipitation characteristics. In addition, there are also distinct differences in the dislocations of different samples, as demonstrated by the TEM and XRD results (Figs. 5 and 6). All these eventually result in the variation of mechanical properties for different samples (Fig. 2).

As for age-hardenable alloys, precipitation strengthening is the predominant strengthening mechanism for Al–Cu–Li alloys. Meanwhile, the contributions from strain hardening, solution strengthening, and grain boundary strengthening also can not be ignored. As a consequence, to clarify the root reasons for the differences in the mechanical properties of different samples, contributions from the different strengthening mechanisms should be fully considered. Generally, the YS of Al alloys (σ_y) can be described by the following equation [57–59]:

$$\sigma_{\rm y} = \Delta \sigma_{\rm B} + M(\Delta \sigma_{\rm D} + \Delta \sigma_{\rm P}) \tag{1}$$

where $\Delta \sigma_{\rm B}$ is the base strength of the alloy; $\Delta \sigma_{\rm D}$ and $\Delta \sigma_{\rm P}$ are the contributions from strain hardening and precipitation strengthening, respectively; M is the Taylor factor of the material.

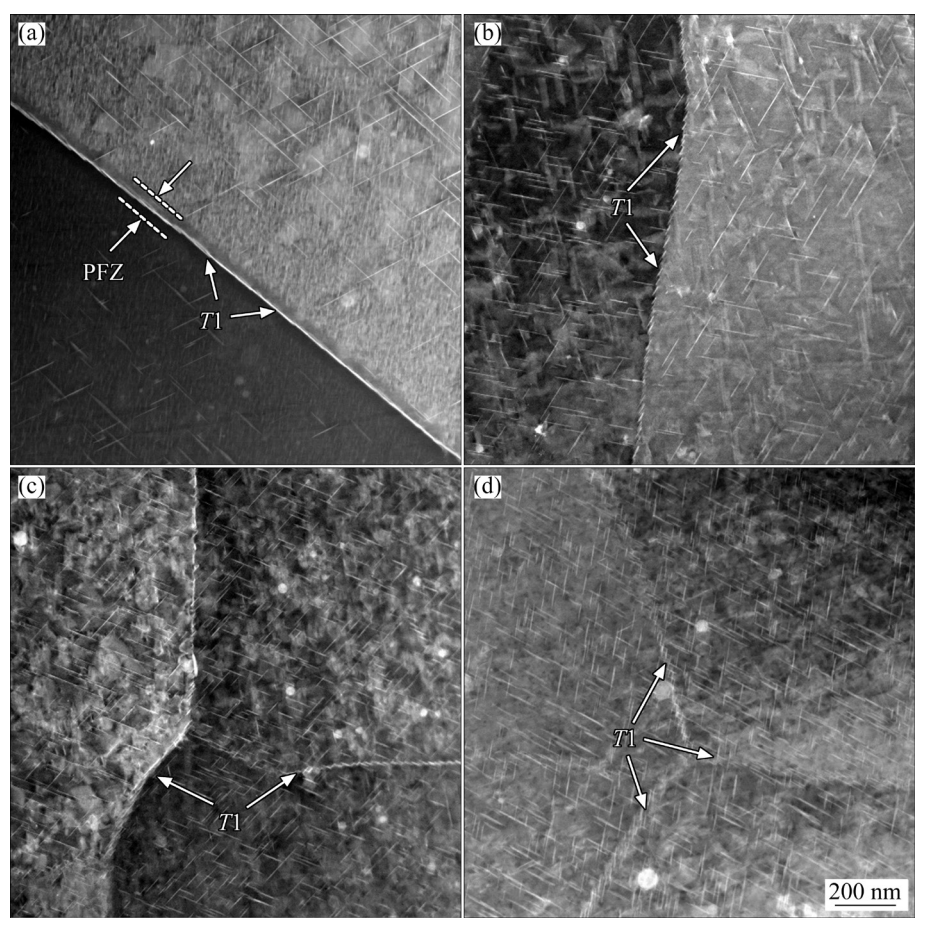


Fig. 11 HAADF-STEM images of grain boundaries/sub-grain boundaries regions in different samples viewed along [110]_{Al} axis zone: (a) T6; (b) T8-3; (c) T8-9; (d) T8-15

4.2.1 Base strength

The base strength ($\Delta\sigma_B$) mainly includes the intrinsic lattice strength ($\Delta\sigma_b$), grain boundary strengthening ($\Delta\sigma_{gb}$), and solid solution strengthening ($\Delta\sigma_{ss}$). The values of $\Delta\sigma_{gb}$ should remain constant for samples with different pre-deformations, as the pre-deformation methods have little impact on the grain sizes of Al–Cu–Li alloys [37,60]. Solution strengthening originates from the interactions between mobile dislocations and solute atoms, which are highly affected by the alloy compositions. For highly alloyed third-generation Al–Cu–Li alloys, solution strengthening contributions can reach 70.0–80.0 MPa [42,61]. It can be roughly estimated by the following equation [62]:

$$\begin{cases} \sigma_{\rm ss}^{\rm X} = A_x C_x^{2/3} \\ \Delta \sigma_{\rm ss} = \sigma_{\rm trace} + \sum \sigma_{\rm ss}^x \end{cases}$$
 (2)

where σ_{ss}^{X} is solution strengthening contribution from one type of solute atom (X); C_x is solute concentration in mass fraction; A_x values for the

major alloying elements (Li, Cu, and Mg) in the experimental alloy are 10.862, 12.132, and 20.481, respectively; σ_{trace} is the contribution from trace elements such as Fe and Si, approximately 24.0 MPa [63,64]. Based on Eq. (2), the solution strengthening value for the experimental alloys is calculated to be about 75.0 MPa.

In many studies, the value of $\Delta \sigma_B$ for the artificially aged alloys is roughly considered to be equivalent to the YS of the as-quenched alloys [37,39,65]. This is mainly based on the assumption that the loss of solution strengthening can be ignored in comparison to the high increment of precipitation strengthening during the aging process. However, LV et al [66] found that there was a deviation of up to 40.0 MPa between the theoretical calculation strength and the experimental results of the T8-aged 2195 Al–Cu–Li alloy, based on this hypothesis. Actually, in agehardenable Al alloys, the formation of precipitates undoubtedly consumes massive solute atoms in the matrix, which in turn weakens the solution-

strengthening effects. In terms of the investigated Al-Cu-Li alloy, by considering the high solution strengthening value (75.0 MPa) and the complex alloy elements, it is unreasonable to ignore the loss of solution strengthening during the aging process. To obtain a more accurate value of $\Delta \sigma_B$ for the aged alloys, the SFCI sample is utilized. For the SFCI sample, during the furnace cooling stage, an extremely low cooling rate enables the massive formation of the coarse Al-Cu phases with large size (Fig. 4), which almost depletes the solutes in the matrix and therefore weakens the solution strengthening effects. Notably, this state of the SFCI sample is extremely similar to that of the aged alloys, except for the secondary phases. DUAN et al [48] and TANG et al [67] have demonstrated that these micron-sized coarse Al-Cu phases in the SFCI sample formed during the furnace cooling stage are primarily the θ' and T1 precipitates and have a limited impact on the strength of alloys. As expected, the YS of the SFCI sample is 104.6 MPa, which is approximately 62.0 MPa lower than that of the as-quenched sample (165.8 MPa). This value is close to the contribution from solid solution strengthening (75.0 MPa). Therefore, by taking into account the loss of solution strengthening during the aging process, the value of YS for the SFCI sample is more approximate to the actual value of $\Delta \sigma_{\rm B}$ for the aged alloy.

4.2.2 Strain strengthening

Both TEM and XRD measurements reveal that the dislocation density in samples significantly increases with improving the levels of predeformation. Since the moderate aging temperature (~150 °C) can not enable the occurrence of static recovery for the Al–Cu–Li alloy, the strain hardening contribution from pre-deformation is reasonably considered to be constant during the aging process [37]. Strain-hardening contributions can be expressed as follows [23]:

$$\Delta \sigma_{\rm D} = M \alpha G b \rho^{1/2} \tag{3}$$

where α is a constant, G is the shear modulus, b is the magnitude of Burgers vector, and ρ is the dislocation density. According to the dislocation density values in Fig. 6 and Eq. (3), the strain hardening contributions are calculated and given in Fig. 12. As shown, the contributions from strain hardening significantly increase with improving the levels of pre-deformation in samples.

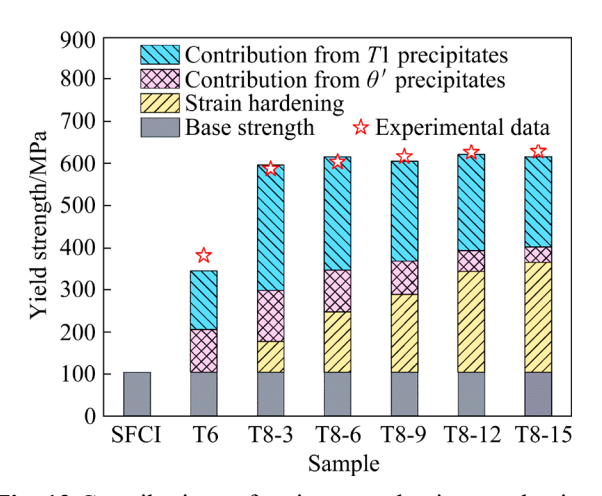


Fig. 12 Contributions of main strengthening mechanisms to yield strength (YS) of samples and comparison between experimental strength and predicted one

4.2.3 Precipitation strengthening

The precipitation strengthening is derived from the precipitates-dislocations interaction, of which the strengthening mechanisms are dependent on the precipitates being bypassed or sheared by the dislocations. As discussed in Section 4.1, T1 and θ' precipitates are the predominant precipitates in the samples after aging treatment. The characteristics of these precipitates such as the type, volume fraction, and size have a great impact on the precipitation strengthening effects. It has been demonstrated that the bypass mechanism is activated for the T1 precipitates with large diameter (>100 nm) or (>1.3 nm) [29,32]. thickness Therefore, modified Orawan model based on the bypass mechanism is employed to predict the contribution $(\Delta \sigma_{P,T1})$ of precipitation strengthening from the T1 precipitates with a large diameter (112.3 nm) in the T6 sample [68]:

$$\Delta \sigma_{P,T1} = \frac{0.12Gb}{\sqrt{Dt}} \left(\sqrt{f_{v}} + 0.7 \sqrt{\frac{D}{t}} f_{v} + 0.12 \frac{D}{t} f_{v}^{3/2} \right) \cdot \ln \left(\frac{0.079D}{b} \right)$$

$$(4)$$

where D, t, and f_v are the diameter, thickness, and volume fraction of precipitates, respectively.

As for the T1 precipitates with smaller diameters (<80 nm) in the T8-X samples, their contributions can be estimated by the model with respect to the shear mechanism proposed by DORIN et al [69]:

$$\Delta \sigma_{P,T1} = \frac{1.211D\gamma_{\text{eff}}^{3/2}}{t^2} \sqrt{\frac{bf_{\text{v}}}{\Gamma}}$$
 (5)

where $\gamma_{\rm eff}$ is the interfacial energy, and Γ is the dislocation line tension (with the value of $Gb^2/2$ approximately).

The bypass mechanism is responsible for the strengthening contribution from θ' precipitates, which can be assessed by the Orawan equation proposed by NIE and MUDDLE [70]:

$$\begin{cases}
\Delta \sigma_{P,\theta'} = \frac{K_{\theta'}}{0.931 \sqrt{\frac{0.306\pi t}{f_v}} \sqrt{D} - \frac{\pi}{8} D - 1.061t} \\
K_{\theta'} = \left\{ \frac{Gb}{2\pi\sqrt{1-v}} \right\} \left\{ \ln \frac{1.225t}{r_0} \right\}
\end{cases}$$
(6)

Figure 12 shows the contributions of the main strengthening mechanisms to the YS of samples with different pre-deformation and the comparison between experimental strength and the predicted one. With increasing the pre-deformation levels in samples, the contribution from strain hardening increases, whereas it diminishes for the precipitation strengthening. Therefore, the increment of the strain hardening contributions is primarily responsible for the increased YS samples with higher pre-deformation levels. Additionally, although the T1 precipitation is significantly enhanced by the increased predeformation, its strength contributions decrease, especially for samples with high pre-deformation levels. DORIN et al [69] have proposed that the variation in diameter of T1 precipitates has a larger impact on the strengthening contribution in comparison to that of number density. Consequently, despite the remarkably increased number density of T1 precipitates, the decrease in their diameter eventually results in their reduced strengthening contributions. Meanwhile, inhibited precipitation of θ' precipitates in samples with the increased pre-deformation leads to a continuous reduction in their strengthening contributions. As a result, the contributions from precipitation strengthening (T1 and θ' precipitates) decrease with increasing levels of pre-deformation in samples. As shown in Fig. 12, the predicted YS of T8-X samples has a good fit for the experimental one. However, the prediction for the T6 sample deviates obviously from the experimental data. This may be related to the neglect of the contributions from the GP zones in the T6 sample (Fig. 8(a)). Indeed, the influence of GP zones on the strength of Al-Cu-Li alloy has been revealed in our previous study [44]. Although the accurate strengthening model for GP zones remains lacking, their strengthening contributions for the T6 sample in this study can not be ignored.

The precipitation behavior of precipitates at the GBs/sub-grain boundary and the interior of the grains has a large impact on the plasticity of the samples. Generally, the presence of PFZs can deteriorate the ductility of the alloy because the stress concentration preferentially occurs in this region during the tensile test [71,72]. Nevertheless, the T6 sample has relatively higher elongation despite the presence of PFZs (Fig. 2 and Fig. 11). In terms of the T6 sample, the small number of precipitates in the grains cause a weakened intragranular strengthening effect. During the tensile tests, the crack propagates preferentially toward the grain interior and shows transgranular fracture with a higher elongation. In addition, the low initial dislocation density in the T6 sample can also delay the occurrence of necking constriction and benefit ductility [23]. For the T8-X samples, pre-deformation weakens the enrichment of T1 precipitates at GBs/sub-grain boundaries, thereby suppressing the formation of PFZ (Fig. 11). This can alleviate the stress concentration levels, and be favored for the improvement of the ductility. However, the high number density of T1 precipitates strongly hinders the movement of dislocations, resulting in dislocation pinning or blockage in the grains. This induces a significant intragranular strengthening effect leading relatively weak grain boundaries. Therefore, tensile failure starts from the grain boundary during tension, exhibiting relatively low elongation for the T8-X samples.

Through the detailed discussion about the various strengthening contributions including base strength, strain hardening, and precipitation strengthening, the intrinsic mechanism for the further strength enhancement of T8-aged Al–Cu–Li alloys with increased pre-deformation is innovatively illustrated. These findings indicate that enhancing the strain hardening contribution while maintaining a high precipitation strengthening contribution is necessary for the development of high-strength Al–Cu–Li alloys. This also provides the theoretical basis and data support for the choice

of alloy strengthening methods for achieving comprehensive performance improvements in Al-Cu-Li alloys.

5 Conclusions

- (1) The increased pre-deformation improves the strength of the Al–Cu–Li alloys but deteriorates the elongations. A tensile strength of about 650.0 MPa with an elongation of 6.0% can be achieved in the sample with a pre-deformation of 15.0%.
- (2) The higher number density of dislocations is introduced in the samples with higher pre-deformation. This suppresses the formation of GP zones and diminishes the θ' precipitates while promoting the nucleation of T1 precipitates. With increasing the pre-deformation, the diameter of both T1 and θ' precipitates decreases obviously, narrowing their size distribution.
- (3) With increasing the pre-deformation, the strength contributions from T1 and θ' precipitates decrease, leading to weakened precipitation strengthening effects. Although the number density of T1 precipitates increases, the reduction of diameter eventually decreases their strength contributions. The increased strain hardening contributions from the higher levels of predeformation are primarily responsible for the improved YS of the alloy. Therefore, it is crucial to increase strain hardening contributions while maintaining high precipitation hardening for the development of high-strength Al-Cu-Li alloys.

CRediT authorship contribution statement

San-xi DENG: Validation, Formal analysis, Investigation, Resources, Writing - Original draft, Writing - Review & editing; Jin-feng LI: Validation, Investigation, Writing - Review & editing; Li WANG: Conceptualization, Writing - Revision, Supervision; CHEN: Methodology, Yue-yan Investigation, Supervision, Conceptualization; Zheng-wu XIANG: Conceptualization, Supervision, Validation, Formal analysis; Peng-cheng MA: Methodology, Investigation, Conceptualization; Yong-lai CHEN: Supervision, Methodology, Investigation, Supervision, Conceptualization; Dan-yang LIU: Validation, Formal analysis, Writing - Review & editing, Funding acquisition, Resources.

Declaration of competing interest

The authors declare that they have no known

competing financial interests or personal relationships that could have appeared to influence the work reported in this paper.

Acknowledgments

This work was supported by the Natural Science Foundation of Hunan Province, China (No. 2023JJ30678).

References

- [1] RIOJA R J, LIU J. The evolution of Al–Li base products for aerospace and space applications [J]. Metallurgical and Materials Transactions A, 2012, 43: 3325–3337.
- [2] EL-ATY A A, XU Yong, GUO Xun-zhong, ZHANG Shi-hong, MA Yan, CHEN Da-yong. Strengthening mechanisms, deformation behavior, and anisotropic mechanical properties of Al–Li alloys: A review [J]. Journal of Advanced Research, 2018, 10: 49–67.
- [3] DURSUN T, SOUTIS C. Recent developments in advanced aircraft aluminum alloys [J]. Materials & Design, 2014, 56: 862–871.
- [4] LU Ding-ding, LIN Ben, LIU Tian-le, DENG San-xi, GUO You-jie, LI Jin-feng, LIU Dan-yang. Effect of grain structure on fatigue crack propagation behavior of Al-Cu-Li alloys [J]. Journal of Materials Science & Technology, 2023, 148: 75-89.
- [5] XU Y B, ZHONG W L, CHEN Y J, SHEN L T, LIU Q, BAI Y L, MEYERS M A. Shear localization and recrystallization in dynamic deformation of 8090 Al–Li alloy [J]. Materials Science and Engineering A, 2001, 299: 287–295.
- [6] HAJJIOUI E A, BOUCHAÂLA K, FAQIR M, ESSADIQI E. A review of manufacturing processes, mechanical properties and precipitations for aluminum lithium alloys used in aeronautic applications [J]. Heliyon, 2023, 9: e12565.
- [7] LI Jin-feng, HUANG Jia-lei, LIU Dan-yang, CHEN Yong-lai, ZHANG Xu-hu, MA Peng-cheng. Distribution and evolution of aging precipitates in Al-Cu-Li alloy with high Li concentration [J]. Transactions of Nonferrous Metals Society of China, 2019, 29: 15-24.
- [8] GUMBMANN E, GEUSER F D, SIGLI C, DESCHAMPS A. Influence of Mg, Ag and Zn minor solute additions on the precipitation kinetics and strengthening of an Al-Cu-Li alloy [J]. Acta Materialia, 2017, 133: 172–185.
- [9] LIU Dan-yang, LI Jin-feng, MA Yun-long, GUPTA R K, BIRBILIS N, ZHANG Rui-feng. A closer look at the role of Zn in the microstructure and corrosion of an Al-Cu-Li alloy [J]. Corrosion Science, 2018, 145: 220-231.
- [10] WANHILL R J H, ESWARA PRASAD N, GOKHALE A A. Aluminum–lithium alloys: Processing, properties, and applications [M]. Boston: Elsevier, 2014.
- [11] DESCHAMPS A, GARCIA M, CHEVY J, DAVO B, GEUSER F D. Influence of Mg and Li content on the microstructure evolution of Al-Cu-Li alloys during long-term ageing [J]. Acta Materialia, 2017, 122: 32-46.
- [12] DECREUS B, DESCHAMPS A, GEUSER F D, DONNADIEU P, SIGLI C, WEYLAND M. The influence of

462 - 472.

- Cu/Li ratio on precipitation in Al-Cu-Li-x alloys [J]. Acta Materialia, 2013, 61: 2207-2218.
- [13] LI Hao-ran, ZOU Zhi-tao, LI Jin-feng, XU Guo-fu, ZHENG Zi-qiao. Correlation between grain structures and tensile properties of Al-Li alloys [J]. Transactions of Nonferrous Metals Society of China, 2023, 33: 3597–3611.
- [14] ZHAO Xin-yue, LIU Wen-sheng, XIAO Dai-hong, MA Yun-zhu, HUANG Lan-ping, TANG Ya. A critical review: Crystal structure, evolution and interaction mechanism with dislocations of nano precipitates in Al–Li alloys [J]. Materials & Design, 2022, 217: 110629.
- [15] GUMBMANN E, LEFEBVRE W, GEUSER F D, SIGLI C, DESCHAMPS A. The effect of minor solute additions on the precipitation path of an Al-Cu-Li alloy [J]. Acta Materialia, 2016, 115: 104–114.
- [16] CHEN Long-hui, MA Pei-pei, LIU Chun-hui, ZHAN Li-hua, ZHENG Ze-yu. A precipitation pathway of *T*1 phase via heterogeneous nucleation on Li-rich particle in Al–Cu–Li alloy [J]. Journal of Alloys and Compounds, 2024, 971: 172796.
- [17] LIU Zhen-zhen, DENG San-xi, RAO Mao, QUE Ji-rong, LI Jin-feng, LIU Dan-yang. Effect of grain thickness and *T*1 precipitate on the strength anisotropy of Al–4.0Cu–1.0Li–0.4Mg–0.4Ag–xZr alloys under different heat treatment [J]. Journal of Alloys and Compounds, 2023, 968: 172105.
- [18] LIU Chun-hui, ZHOU Yi-hui, MA Pei-pei, HE Jun, CHEN Long-hui. Enhanced age-hardening response at elevated temperature by natural-ageing-modified precipitation in an Al-Cu-Li-Mg alloy [J]. Materials Characterization, 2023, 199: 112791.
- [19] MA Yun-long, LI Jin-feng, ZHANG Run-zhe, TANG Jian-guo, HUANG Cheng, LI Hong-ying, ZHENG Zi-qiao. Strength and structure variation of 2195 Al-Li alloy caused by different deformation processes of hot extrusion and cold-rolling [J]. Transactions of Nonferrous Metals Society of China, 2020, 30: 835–849.
- [20] YOSHIMURA R, KONNO T J, ABE E, HIRAGA K. Transmission electron microscopy study of the early stage of precipitates in aged Al-Li-Cu alloys [J]. Acta Materialia, 2003, 51: 2891–2903.
- [21] NING Hong, LI Jin-feng, MA Peng-cheng, CHEN Yong-lai, ZHANG Xu-hu, ZHANG Kai, ZHANG Rui-feng. Evolution of aging precipitates in an Al–Li alloy with 1.5 wt.% Li concentration [J]. Vacuum, 2020, 182: 109677.
- [22] ZHANG Xiao-long, ZHANG Liang, WU Guo-hua, LIU Wen-cai, SHI Chun-chang, TAO Jia-shen, SUN Jiang-wei. Microstructural evolution and mechanical properties of cast Al-2Li-2Cu-0.5Mg-0.2Zr alloy during heat treatment [J]. Materials Characterization, 2017, 132: 312-319.
- [23] XIE Yuan-kang, LIU Sheng-dan, GUO Xiao-bin, DENG Yun-lai. Development of ultra-high strength Al-Cu-Li alloys containing high Mg through the combination of pre-stretching and age-hardening [J]. Materials Science and Engineering A, 2024, 896: 146289.
- [24] DONNADIEU P, SHAO Y, GEUSER F D, BOTTON G A, LAZAR S, CHEYNET M, de BOISSIEU M D, DESCHAMPS A. Atomic structure of *T*1 precipitates in Al–Li–Cu alloys revisited with HAADF-STEM imaging and small-angle X-ray scattering [J]. Acta Materialia, 2011, 59:

- [25] MARTIN J W. Precipitation hardening [M]. 2nd ed. Boston: Elsevier, 1998.
- [26] ZENG Guang-jun, NING Hong, DENG San-xi, LI Jin-feng, YAO Yong, GUO You-jie, LU Ding-ding, LI Yu-zhuo, LIU Zhi-hao, MA Peng-cheng, ZHANG Rui-feng. Quantification of the effect of increased pre-deformation on microstructure and mechanical properties of 2A55 Al-Li alloy [J]. Advanced Engineering Materials, 2022, 24: 2200033.
- [27] LV Pin-hui, WANG Ri-chu, PENG Chao-qun, CAI Zhi-yong, FENG Yan, WANG Xiao-feng. Precipitation and mechanical properties for rapidly solidified Al-Cu-Li alloy: Effect of pre-rolling [J]. Journal of Alloys and Compounds, 2022, 929: 167369.
- [28] XIE Bing-xin, HUANG Liang, XU Jia-hui, SU Hong-liang, ZHANG Hui-ping, XU Yi-ke, LI Jian-jun, WANG Yu. Effect of the aging process and pre-deformation on the precipitated phase and mechanical properties of 2195 Al–Li alloy [J]. Materials Science and Engineering A, 2022, 832: 142394.
- [29] GUO Guang-yi, LI Yao, LI Hao-ran, PENG Xiao-yan, LI Jin-feng, XU Guo-fu. Quantitative effects of pre-deformation prior to non-isothermal aging on the mechanical properties—microstructure relationships in an Al-3.51Cu-1.01Li alloy [J]. Materials & Design, 2022, 223: 111137.
- [30] TSIVOULAS D, PRANGNELL P B. Comparison of the Effect of individual and combined Zr and Mn additions on the fracture behavior of Al-Cu-Li alloy AA2198 rolled sheet [J]. Metallurgical and Materials Transactions A, 2014, 45: 1338-1351.
- [31] XU Jin-jun, DENG Yun-lai, CHEN Ji-qiang, XIE Yuan-kang, GUO Xiao-bin. Effect of ageing treatments on the precipitation behavior and mechanical properties of Al-Cu-Li alloys [J]. Materials Science and Engineering A, 2020, 773: 138885.
- [32] WANG Xiao-ming, SHAO Wen-zhu, JIANG Jian-tang, LI Guo-ai, WANG Xiao-ya, ZHEN Liang. Quantitative analysis of the influences of pre-treatments on the microstructure evolution and mechanical properties during artificial ageing of an Al-Cu-Li-Mg-Ag alloy [J]. Materials Science and Engineering A, 2020, 782: 139253.
- [33] GABLE B M, ZHU A W, CSONTOS A A, STARKE E A. The role of plastic deformation on the competitive microstructural evolution and mechanical properties of a novel Al-Li-Cu-X alloy [J]. Journal of Light Metals, 2001, 1: 1–14.
- [34] CASSADA W A, SHIFLET G J, STARKE E A. The effect of plastic deformation on Al₂CuLi (*T*1) precipitation [J]. Metallurgical Transactions A, 1991, 22: 299–306.
- [35] DUAN Shu-wei, GUO Fu-qiang, WU Dong-ting, WANG Tao, TSUCHIYA T, MATSUDA K, ZOU Yong. Influences of pre-rolling deformation on aging precipitates and mechanical properties for a novel Al-Cu-Li alloy [J]. Journal of Materials Research and Technology, 2021, 15: 2379–2392.
- [36] LI Yao, XU Guo-fu, QIAO Hai-guang, LIU Shi-chao, PENG Xiao-yan. Effect of pre-deformation on microstructure and mechanical properties of 2050 Al–Li alloy [J]. Transactions of Nonferrous Metals Society of China, 2024, 34: 1774–1788.

- [37] RODGERS B I, PRANGNELL P B. Quantification of the influence of increased pre-stretching on microstructurestrength relationships in the Al-Cu-Li alloy AA2195 [J]. Acta Materialia, 2016, 108: 55-67.
- [38] DORIN T, GEUSER F D, LEFEBVRE W, SIGLI C, DESCHAMPS A. Strengthening mechanisms of T1 precipitates and their influence on the plasticity of an Al-Cu-Li alloy [J]. Materials Science and Engineering A, 2014, 605: 119–126.
- [39] LV Pin-hui, WANG Ri-chu, PENG Chao-qun, CAI Zhi-yong. Improved strength and ductility of rapidly solidified 2195 alloy by pre-rolling combined with double aging and interrupted aging [J]. Materials Science and Engineering A, 2023, 873: 145023.
- [40] DUMONT M, LEFEBVRE W, DOISNEAU-COTTIGNIES B, DESCHAMPS A. Characterisation of the composition and volume fraction of η' and η precipitates in an Al–Zn–Mg alloy by a combination of atom probe, small-angle X-ray scattering and transmission electron microscopy [J]. Acta Materialia, 2005, 53: 2881–2892.
- [41] JIANG Bo, WANG Hai-sheng, YI Dan-qing, TIAN Yu, SHEN Fang-hua, WANG Bin, LIU Hui-qun, HU Zhan. Effect of Ag addition on the age hardening and precipitation behavior in an Al-Cu-Li-Mg-Zn-Mn-Zr alloy [J]. Materials Characterization, 2020, 162: 110184.
- [42] ZENG Guang-jun, LI Hao-ran, DENG San-xi, MA Peng-cheng, CHEN Yong-lai, LIU Tian-le, LI Jin-feng, LIU Dan-yang, XU Guo-fu. Detailed investigation on microstructure and strengthening contribution of Al-xCu-1.3Li-X alloy sheets [J]. Materials Characterization, 2023, 205: 113278.
- [43] YUZBEKOVA D, MOGUCHEVA A, ZHEMCHUZHNIKOVA D, LEBEDKINA T, LEBYODKIN M, KAIBYSHEV R. Effect of microstructure on continuous propagation of the Portevin-Le Chatelier deformation bands [J]. International Journal of Plasticity, 2017, 96: 210–226.
- [44] DENG San-xi, LIU Zhen-zhen, ZENG Guang-jun, XIANG Hui, MA Peng-cheng, YIN Jia-ming, KANG Li, WEN Si-han, LI Jin-feng, LIU Dan-yang. The precipitation evolution and mechanical properties of an Al-Cu-Li-Mg alloy during natural aging [J]. Journal of Materials Science & Technology, 2024, 192: 42–53.
- [45] WANG Cheng, ZHANG Jin, ZHU Chun-nan, YI You-ping. Multi slip activation enabled excellent low-temperature strength-ductility synergy in Al-Cu-Li alloy [J]. Vacuum, 2022, 204: 111328.
- [46] XU Cong, ZHENG Rui-xiao, HANADA Shu-ji, XIAO Wen-long, MA Chao-li. Effect of hot extrusion and subsequent T6 treatment on the microstructure evolution and tensile properties of an Al-6Si-2Cu-0.5Mg alloy [J]. Materials Science and Engineering A, 2018, 710: 102-110.
- [47] LI Quan, WANG Jun-sheng, LIU Xin-xiu, XUE Cheng-peng, WANG Shuo, YANG Xing-hai, TIAN Guang-yuan, SU Hui, WU Xue-long, MIAO Yi-sheng. Accelerating the dissolution and transformation of detrimental Fe-rich intermetallics in recycled Al–Mg–Si alloy by homogenization and hot deformation [J]. Materials Characterization, 2024, 213: 114024.
- [48] DUAN Shu-wei, GUO Fu-qiang, QIN Shuai-shuai, GAO Yu,

- MATSUDA K, ZOU Yong. Effects of cooling rates on precipitates in homogenized Al-Cu-Li alloy [J]. Materials Letters, 2021, 293: 129695.
- [49] GUO You-jie, LI Jin-feng, LU Ding-ding, DENG San-xi, ZENG Guang-jun, MA Yun-long, YOU Wen, CHEN Yong-lai, ZHANG Xu-hu, ZHANG Rui-feng. Characterization of Al₃Zr precipitation via double-step homogenization and recrystallization behavior after subsequent deformation in 2195 Al–Li alloy [J]. Materials Characterization, 2021, 182: 111549.
- [50] DENG San-xi, LI Jin-feng, NING Hong, LU Ding-ding, ZENG Guang-jun, LIU Zhen-zhen, XIANG Hui, QUE Ji-rong, LIU Dan-yang. Effect of Zr addition on the microstructure evolution and mechanical properties of extruded Al-Cu-Li-Mn alloys [J]. Materials Characterization, 2023, 202: 113011.
- [51] KRÁLÍK R, KŘIVSKÁ B, BAJTOŠOVÁ L, STOLBCHENKO M, SCHAPER M, GRYDIN O, CIESLAR M. Effect of Sc addition on downstream processing of twinroll cast Al-Cu-Li-Mg-Zr-based alloys [J]. Transactions of Nonferrous Metals Society of China, 2024, 34: 1759-1773.
- [52] CHUNG T F, YANG Y L, HSIAO C N, LI W C, HUANG B M, TSAO C S, SHI Zhu-sheng, LIN Jian-guo, FISCHIONE P E, OHMURA T, YANG J R. Morphological evolution of GP zones and nanometer-sized precipitates in the AA2050 aluminium alloy [J]. International Journal of Lightweight Materials and Manufacture, 2018, 1: 142–156.
- [53] XU Xuan-xi, WU Guo-hua, ZHANG Liang, TONG Xin, ZHANG Xiao-long, SUN Jiang-wei, LI Liang-bin, XIONG Xun-man. Effects of heat treatment and pre-stretching on the mechanical properties and microstructure evolution of extruded 2050 Al-Cu-Li alloy [J]. Materials Science and Engineering A, 2022, 845: 143236.
- [54] GUTIÉRREZ-URRUTIA I. Study of isothermal δ'(Al₃Li) precipitation in an Al–Li alloy by thermoelectric power [J]. Journal of Materials Science, 2011, 46: 3144–3150.
- [55] UNLU N, GABLE B M, SHIFLET G J, STARKE E, STÅL Ö. The effect of cold work on the precipitation of Ω and θ' in a ternary Al–Cu–Mg Alloy [J]. Materials Science Forum, 2002, 396/397/398/399/400/401/402: 801–806.
- [56] MA Pei-pei, ZHAN Li-hua, LIU Chun-hui, WANG Qing, LI He, LIU De-bo, HU Zheng-gen. Pre-strain-dependent natural ageing and its effect on subsequent artificial ageing of an Al-Cu-Li alloy [J]. Journal of Alloys and Compounds, 2019, 790: 8–19.
- [57] STARINK M J, WANG S C. A model for the yield strength of overaged Al–Zn–Mg–Cu alloys [J]. Acta Materialia, 2003, 51: 5131–5150.
- [58] LIU Shi-chao, XU Guo-fu, LI Yao, LI Hao-ran, PENG Xiao-yan. Detailed investigation on high-temperature mechanical properties of AA2050 Al-Cu-Li alloys [J]. Materials Science and Engineering A, 2022, 844: 143158.
- [59] XIE Yuan-kang, LIU Sheng-dan, GUO Xiao-bin, LIANG Chao-jie, DENG Yun-lai. Enhancing the strength of Sc-containing Al-Cu-Li alloys by modifying the precipitation behavior through plastic deformation and heat treatment [J]. Materials Characterization, 2024, 207: 113558.
- [60] YE Fan, YU You-xing, ZHANG Bao-shuai, RONG Jian, HE Dong-lei, HAN Bao-shuai, MA Xiao-guang, ZENG Yuan-

- song, XU Yan-jin, WU Su-jun. Influence of pre-stretching at ambient and cryogenic temperatures on dislocation configuration, precipitation behavior, and mechanical properties of 2195 Al–Cu–Li alloy [J]. Journal of Materials Research and Technology, 2023, 22: 2983–2995.
- [61] ZHU Zhi-xiong, HAN Jian, GAO Chong, LIU Mao, SONG Jian-wei, WANG Zhi-wei, LI Hui-jun. Microstructures and mechanical properties of Al-Li 2198-T8 alloys processed by two different severe plastic deformation methods: A comparative study [J]. Materials Science and Engineering A, 2017, 681: 65-73.
- [62] TOTTEN G E, MACKENZIE D S, Handbook of aluminum: Physical metallurgy and processes [M]. Florida: Taylor & Francis, 2003.
- [63] DENG Yun-lai, XU Jin-jun, CHEN Ji-qiang, GUO Xiao-bin. Effect of double-step homogenization treatments on the microstructure and mechanical properties of Al-Cu-Li-Zr alloy [J]. Materials Science and Engineering A, 2020, 795: 139975.
- [64] HUSKINS E L, CAO B, RAMESH K T. Strengthening mechanisms in an Al-Mg alloy [J]. Materials Science and Engineering A, 2010, 527: 1292–1298.
- [65] XU Xuan-xi, WU Guo-hua, ZHANG Liang, TONG Xin, QI Fang-zhou, GUO You-jie, LI Liang-bin, XIONG Xun-man, WANG Cun-long. Regulation of precipitation behavior among T1, S', and θ' phases in Al-Cu-Li-(Mg-Ag) alloys by optimizing Ag/Mg ratios [J]. Materials Science and Engineering A, 2023, 876: 145158.
- [66] LV Pin-hui, WANG Ri-chu, PENG Chao-qun, CAI Zhi-yong. Microstructural evolution and mechanical properties of 2195

- Al-Li alloy processed by rapid solidification and thermomechanical processing [J]. Journal of Alloys and Compounds, 2023, 948: 169794.
- [67] TANG Ya, XIAO Dai-hong, HUANG Lan-ping, YOU Ren-xuan, ZHAO Xin-yue, LIN Nan, MA Yun-zhu, LIU Wen-sheng. Effect of minor Sc addition on the microstructure evolution of Al-Cu-L-Mg alloy during homogenization with different cooling Modes [J]. Metals and Materials International, 2022, 28: 2422-2433.
- [68] Zhu A W, CSONTOS A, STARKER E A. Computer experiment on superposition of strengthening effects of different particles [J]. Acta Materialia, 1999, 47: 1713–1721.
- [69] DORIN T, DESCHAMPS A, GEUSER F D, SIGLI C. Quantification and modelling of the microstructure/strength relationship by tailoring the morphological parameters of the T1 phase in an Al-Cu-Li alloy [J]. Acta Materialia, 2014, 75: 134-146.
- [70] NIE Jian-feng, MUDDLE B C. Microstructural design of high-strength aluminum alloys [J]. Journal of Phase Equilibria, 1998, 19: 543–551.
- [71] WANG Meng, ZHAN Li-hua, YANG You-liang, YANG Ling, HUANG Ming-hui. Effect of pre-deformation on aging creep of Al-Li-S4 alloy and its constitutive modeling [J]. Transactions of Nonferrous Metals Society of China, 2015, 25: 1383-1390.
- [72] XIAO Zhu, WANG Wei-yang, LEI Qian, YANG Biao-biao, WANG Meng, YANG Yi-hai, ZHOU Da-ren, LI Zhou. Effect of equal channel angular pressing on microstructure evolution and properties variations of a CuCrZrY alloy [J]. Journal of Alloys and Compounds, 2022, 894: 162284.

T8 时效铝铜锂合金随预变形增加的强化机制

邓三喜1,李劲风1,王理2,陈月雁2,向正武1,马鹏程3,陈永来3,刘丹阳1

- 1. 中南大学 材料科学与工程学院,长沙 410083;
 - 2. 西南铝业有限责任公司, 重庆 401326;
 - 3. 航天材料及工艺研究所, 北京 100076

摘 要:研究随预变形量增加(0~15%)时 T8 时效态铝铜锂合金的显微组织演变和力学性能,揭示显微组织特征与强度之间的关系以及内在的强化机制。结果表明,增加预变形量可显著提高该合金的强度但会降低其塑性。预变形引入的位错有效抑制 GP 区的形成,并为 T1 相提供更多形核位点,这导致预变形量更大的样品中形成更密集且细小的 T1 相;同时,T1 相析出增强与 GP 区形成受阻导致 θ 析出相的数量和尺寸显著降低。对不同强化机制的贡献进行定量描述。结果表明:随着预变形量增加,T1 相和 θ 相的强化贡献降低。T1 相直径减小是其强化效果减弱的主要原因。因此,该合金强度的提高主要归因于增加预变形量诱发应变硬化主导的强化贡献。

关键词: 铝铜锂合金; 预变形; 析出; 强度; 强化机制

(Edited by Bing YANG)